Hybrid Ni–Co–Ni Structures Prepared by Magnetophoresis as Efficient Permanent Magnets for Integration into Microelectromechanical Systems

Pierre Moritz, Ilona Lecerf, Antoine Gonon, Georgiana Maties, Thomas Blon, Simon Cayez, David Bourrier, Fabrice Mathieu, José Elías Angulo-Cervera, Liviu Nicu, et al.

Hybrid Ni-Co-Ni Structures Prepared by Magnetophoresis as Efficient Permanent Magnets for Integration into Micro-Electro-Mechanical-Systems

*Pierre Moritz, Ilona Lecerf, Antoine Gonon, Georgiana Dragomir-Maties, Thomas Blon, Simon Cayez, David Bourrier, Fabrice Mathieu, José Elías Angulo-Cervera, Liviu Nicu, Thierry Leïchlé, Thierry Ondarçuhu, Guillaume Viau, Lise-Marie Lacroix**

P. Moritz, I. Lecerf, A. Gonon, G. Dragomir-Maties, T. Blon, S. Cayez, G. Viau and L.-M. Lacroix : Université de Toulouse, Laboratoire de Physique et Chimie des Nano-Objets, UMR 5215 INSA, CNRS, UPS, 135 avenue de Rangueil 31077 Toulouse, France

P. Moritz, I. Lecerf, D. Bourrier, F. Mathieu, J. E. Angulo-Cervera, L. Nicu and T. Leïchlé : LAAS-CNRS, 7 avenue du Colonel Roche, 31077 Toulouse, France

A. Gonon and T. Ondarçuhu : Institut de Mécanique des Fluides de Toulouse, Université de Toulouse, 2 allée du Pr. Camille Soula, 31400 Toulouse, France

T. Leïchlé : Georgia Tech-CNRS International Research Laboratory, School of Electrical and Computer Engineering, Atlantic Drive, Atlanta, GA, 30332, USA

Corresponding author : lmlacroi@insa-toulouse.fr, Tel: +33567048833, Fax: +33561559697

Keywords : nanostructured materials; integrated magnets; magnetophoresis; nanorods; self-assembly; electromagnetic actuation

Abstract : The direct integration of performant permanent magnets within miniaturized circuits remains both a scientific and a technological challenge. Magnetophoresis-driven capillary assembly of hard magnetic nanoparticles is a promising approach to fabricate 3D rare-earth free permanent magnets. However, this process implies the use of soft magnetic blocks to generate the magnetic field gradients required to localize the assembly directly onto silicon substrates. The impact of these soft elements onto the overall magnetic properties was evaluated using Co nanorods as hard material and 150µm thick-Ni blocks. As expected, the presence of Ni softens the overall properties of the hybrid magnet obtained, but permanent magnet properties are preserved for reduced Ni volumes. A magnetic induction as high as 19 mT at a distance of 200 µm is generated by the hybrid Ni-Co-Ni structures, allowing for the electromagnetic actuation of a MEMS resonant sensor.

Introduction :

The societal demand for the upcoming digital society requires the development of miniaturized electronic devices such as Microelectromechanical Systems (MEMS) and the derived biosensors.[1,2,3] As reviewed in 2019,[4] the development of sustainable micro energy sources for these portable devices is not yet achieved despite intensive efforts. The magnetic flux density available being independent of the size, permanent magnets (PM) represent the most attractive choice for miniaturized magnetic power sources. The main limitation arises from a lack of mature permanent magnet technologies for MEMS.[4] Permanent magnets are micro or nano-structured materials designed to generate quasi-perpetual magnetic fields outside their volume, known as stray fields, without requiring any additional external power sources. Their strength, characterized by the energy product – or $(BH)_{max}$,[5] depends on several intrinsic and extrinsic parameters.[6] To reach a significant value, the chosen material should display a high remanent magnetization (Mr) and a high coercivity (H_C), to prevent demagnetization from occurring. Then, the spatial distribution of the stray field strongly depends on the magnet volume, large PM volumes allow preventing the rapid decay of the stray field intensity with distance.

Downsizing PM based on classical metallurgical processes yields high performance rare-earth (RE) based magnets but is incompatible with a monolithic integration on Si-based circuit process flows, due to thermal and mechanical constraints.[7] Alternative approaches have been intensively sought. Important efforts have been devoted to the controlled deposition of thick films (up to a few tens of µm in thickness) of RE-based magnets using sputtering deposition.[8] By combining classical micro-fabrication processes with high rate triode sputtering, Nora Dempsey's group prepared RE micro-magnets using topographically patterned substrates.[8,9] The in-plane dimensions of the micro-magnets were in the range of 10-100 µm, while thicknesses up to 50 µm were achieved for topographically patterned NdFeB films.[10] Alternatively, thermomagnetic patterning process has been developed in which the

nanostructured magnets are locally irradiated with a laser under an external magnetic field.[9,11,12]

To gain access to even thicker magnets, the electroplating technique was used. However, up to now, RE-based material could not be grown by this approach, limiting the studies to material exhibiting moderate coercivity and remanent induction, such as CoNiMnP,[13] or to Pt-based alloys.[14,15] However, post-deposition annealing steps at high temperature (above 650°C) are mandatory to crystallize the proper $L1_0$ tetragonal structures, thus limiting their integration in the process flow of microelectronic fabrication. Alternatively, composite materials consisting of ferromagnetic powders, such as Co[16] or NdFeB particles,[17] embedded within polymers were developed.[18,19] The thick magnets (~50 µm) obtained exhibit however fairly poor magnetic properties due to the dilution of the magnetic powder. As the magnet induction scales with the square of the magnetic volume fraction (f_V),[20] poor $(BH)_{max}$ are obtained. To overcome this limitation, the doctor-blade technique was used to dry-press[21] or wet-deposit[22] micrometric NdFeB particles into pre-etched cavities in a substrate. The high forces observed during solvent evaporation allowed to reach f_V of nearly 80%. These results still suffer from the isotropic character of the magnets, and oxidation issues with NdFeB microparticles.

Nanochemistry has recently made some decisive contributions in the field of hard magnetic materials and PM by controlling the anisotropic growth of single domain and single crystal magnetic nanorods (NR), which exhibit high coercivity at room temperature.[23] Single-domain cobalt NR, prepared by organometallic chemistry[24] or polyol process,[25,26] combine shape and magnetocrystalline anisotropies. Thanks to their small diameter, which favors uniform magnetization reversal, and their very good crystallinity, which limits the nucleation of magnetization reversal on structural defects,[27] these objects exhibit coercivity close to the theoretical anisotropy field $H_a = \frac{2K_1}{M_S} + 2\pi M_S$, with K_1 the magnetocrystalline constant of cobalt and M_S its saturation magnetization, the $2\pi M_S$ term being related to the shape

anisotropy. We have previously demonstrated that dense and parallel assemblies of these Co NRs can make performant PM, filling a gap between the hexaferrites and the RE-based PM.[28,29] Synthesized under air, these Co NRs are naturally passivated by a 1.2 nm thick Co oxide layer, preventing them from further oxidation, leading to stable magnetic properties.[28] Moreover, submillimeter Co NR-based PM integrated in MEMS devices have been fabricated by a fairly simple magnetophoresis process fully compatible with the microelectronics workflow process.[30] In this process, a concentrated suspension of Co NRs was aligned under an external magnetic field and locally attracted toward predefined Ni blocks which induced strong field gradients. The final densification during the drying step yield fairly compact PM with good mechanical properties. The Ni blocks could be manually removed from the substrate applying locally a mechanical pressure. The strong cohesion of the Co NR-based PM allowed preserving the material on the substrate. The Co NR-based PM was then fully characterized and further integrated onto a MEMS resonator, allowing for its electromagnetic actuation.[30] However, the manual removal of Ni blocks can not be seen as a feasible strategy for an industrial perspective. The use of wet etching might be difficult due to the fairly similar chemical properties of Ni and Co, which may result in the damaging of the Co NR assembly.

Therefore, we report here a detailed study on the hybrid Ni-Co-Ni structures. While magnetic multilayers composed of thin nanostructured materials have been widely studied in spintronic devices,[31,32] we focus her on the permanent magnet applications. After a brief overview of the magnetophoresis assembly theory, the effect of the Ni blocks on the magnetic properties of the hybrid PM is discussed.

Magnetophoresis assembly theory

In the presence of an external inhomogeneous magnetic field, the magnetophoretic force applies, allowing for the attraction and the capture of particles at the high flux gradient region: $\overrightarrow{F_m} = (\vec{m}.\nabla)\vec{B}$ with $\vec{m}$ the moment of the particles.

A PM fabrication process based on magnetophoresis-assembly of Co NRs was recently reported.[30] It implies the controlled evaporation of a Co NR suspension under an external magnetic field on a patterned substrate consisting of pairs of electrodeposited Ni blocks, as schematized in Fig. 1a-c. The magnetically soft Ni blocks effectively serve as flux concentrators inducing local magnetic field gradients.

Several forces apply to the Co NRs as schematized in Fig. 1d-e. The buoyancy $\overrightarrow{F_b}$ acts in opposition to the gravitational force $\overrightarrow{F_g}$ which lead to sediment them. The external magnetic field induces a torque on the Co NRs and aligned them. A magnetophoretic force $\overrightarrow{F_m}$ applies then on the ferromagnetic particles and eventually displaces them toward the large magnetic field gradient areas. The surrounding solvent induces a drag force $\overrightarrow{F_d}$ in the opposite direction: $\overrightarrow{F_d} = C.\overrightarrow{v_{mag}}$ with *C* the drag coefficient and $\overrightarrow{v_{mag}}$ the magnetically induced velocity.

Finally, as the solvent evaporation occurs, capillary forces $\overrightarrow{F_c}$ provoke the contraction of the assembly, yielding a fairly compact nanostructured material.

To promote a controlled assembly at the vicinity of the Ni blocks, the magnetic-driven convection should overcome the thermal diffusion. The Peclet number (*Pe*) allows quantifying the relative importance of each contribution and reads as follow :

$$Pe = \frac{v_{mag}.L}{D} \quad \text{(Eq. 4)},$$

with *L* the typical dimension of the particle (length for a nanorod, diameter for a sphere) and *D* the diffusivity of the NP in the solvent. Magnetic convection is predominant for *Pe* >1, thus for large magnetic velocity.

Considering a simple model of non-interacting Co NRs, the magnetic velocity can be determined from classical Newtonian dynamics, considering that gravity force and buoyancy are negligible and that the steady-state is reached ($\overrightarrow{F_d} + \overrightarrow{F_m} = \vec{0}$). The velocity then reads $v_{mag} = \frac{F_m}{C}$ and therefore scales with the magnetic field gradients.

Co NRs being anisotropic particles, the drag coefficient and the diffusivity have two distinct components, parallel and perpendicular to the rod long axis.[30] Therefore, two critical magnetic field gradients necessary to favor the convective motion both parallel and perpendicular can be determined numerically taking in consideration the Co NR size. Magnetic field gradients of few hundred T.m^{-1} (700 T.m^{-1} and 200 T.m^{-1}, respectively) were determined for isolated NR of 16 nm diameter and 180 nm length (Figure S1).[30]

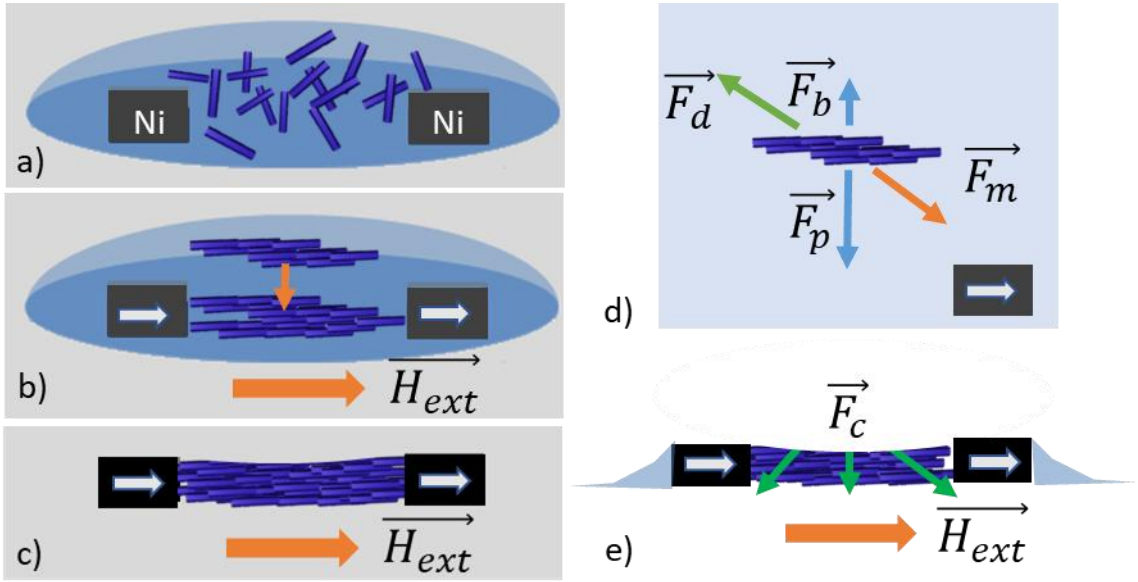

Figure 1. Schematic views of the PM fabrication process : a) Co NR suspension drop-casted on a pair of Ni blocks, b) alignment under external magnetic field and attraction towards the magnetized Ni blocks by magnetophoresis, c) dense assembly obtained after the complete solvent evaporation. d-e) Schematic view of the different forces induced on Co NR chains formed in liquid state under an external magnetic field. $\overrightarrow{F_m}$: magnetophoretic forces, $\overrightarrow{F_d}$: solvent dragging force, $\overrightarrow{F_p}$: weight, $\overrightarrow{F_b}$: buoyancy, $\overrightarrow{F_c}$: capillary forces.

Note that the analysis above is based on a balance of force on isolated NRs particles. Yet, an aggregation of particles in the form of needles is possible at the onset of the magnetic field due to the attractive interactions between aligned Co NRs (see Fig. 1b). This may lead to the formation of needles as in the case of spherical nanoparticles. This would imply a decrease of the Peclet number resulting from larger velocity, larger size and smaller diffusion coefficient. As a result of these collective effects, the critical field gradient required to observe magnetophoresis may be decreased compared to the values given above.[33]

Results and discussion :

Magnetic properties of the Ni blocks

Ni blocks were electroplated on a silicon substrate in order to serve as flux concentrators once placed in a homogeneous external magnetic field (Figure 2). Their length (l) was varied between 100 µm to 1000 µm while their width (w = 500 µm), height (h = 150 µm) and interspacing (Δx = 500µm) were kept constant. The Ni blocks exhibit a saturation magnetization close to the bulk value (500±10 kA.m^{-1}). As expected, the in-plane susceptibility χ_m and the saturation field $\mu_0 H_{sat}$ measured along $\vec{x}$, i.e. the direction joining the 2 blocks, strongly varied with the form factor of the blocks (Figure 2c-d and Table 1).

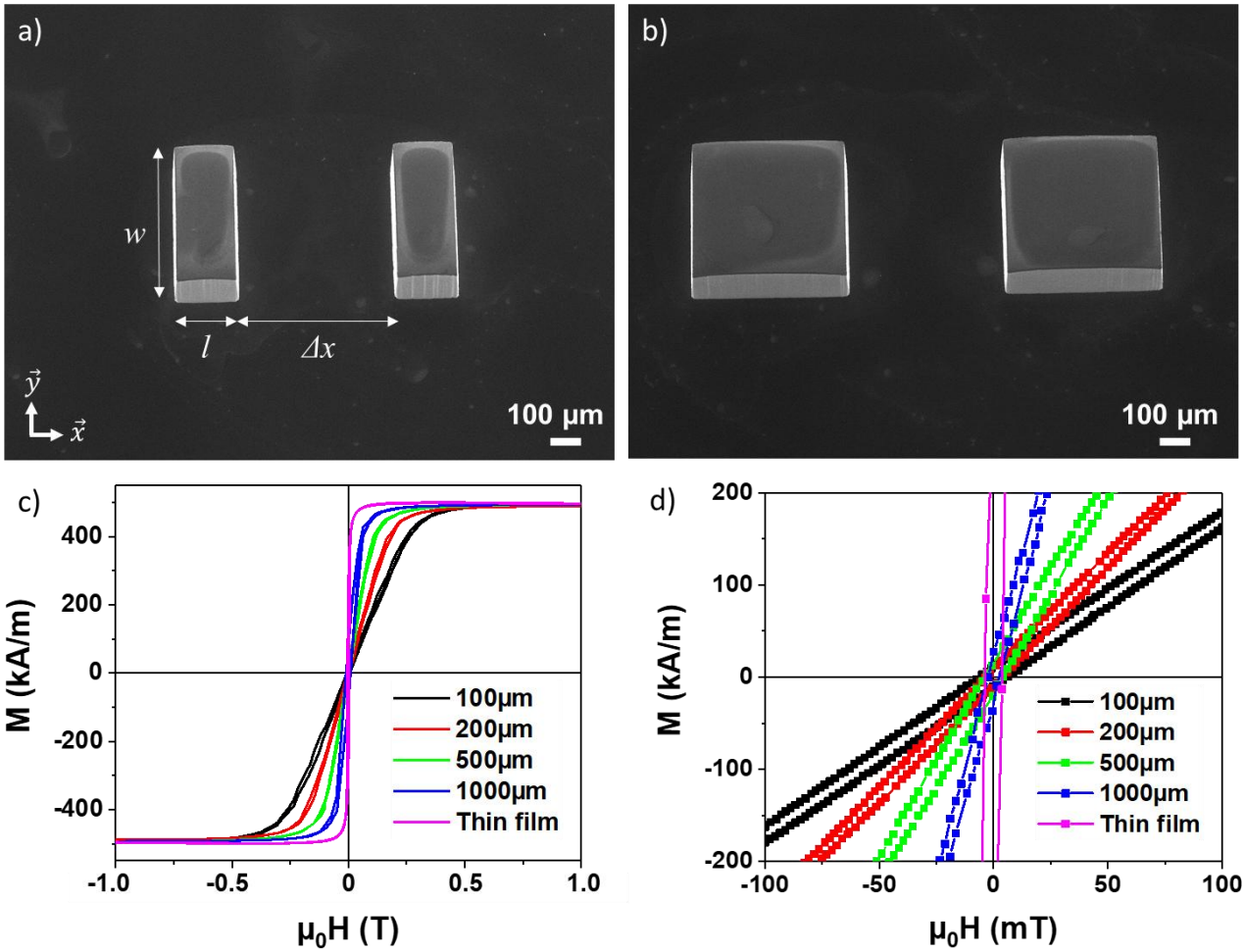

Figure 2. Scanning Electron Microscopy (SEM) images of the Ni blocks with a length *l* of a) 200 µm and b) 500 µm. c) In-plane magnetization curves *M* of Ni blocks of different lengths (*l* = 100 to 1000 µm) and a 5µm thick-Ni thin film measured at 300K along the $\vec{x}$ direction depicted in a. d) zoom on the central part of c) graph.

	Ni blocks			**Ni-Co-Ni hybrid structures**	
Length *l* (µm)	M_s (kA.m^{-1})	$\mu_0 H_{sat}$ (mT)	χ_m	$\mu_0 H_c$ (mT)	m_r/m_{3T}
100	510	390	2	250	0.55
200	505	285	3	150	0.48
500	495	220	5	80	0.50
1000	490	135	10	30	0.37
Thin film	490	40	110	-	-

Table 1. In plane magnetic properties measured along $\vec{x}$ at 300K for different Ni blocks and a 5 µm thick Ni thin film electrodeposited, as reference, and for the hybrid Ni-Co-Ni structures. M_s : saturation magnetization, $\mu_0 H_{sat}$: saturation field. It corresponds to the magnetic field at which the magnetization $m = 0.95\ m_s$, χ_m : in-plane magnetic susceptibility as : $\chi_m = \frac{\partial m}{\partial H}\Big|_{H=0}$. $\mu_0 H_c$: coercive field; m_r/m_{3T} : remanence ratio.

The magnetic field gradients induced by the Ni blocks with lengths of 100, 200 and 500 µm were numerically studied for an external magnetic field $\mu_0 H_{ext} = 1$ T along $\vec{x}$, classically used in this study. As shown in Fig. 3, fairly similar spatial distributions of the magnetic gradients were determined, maxima values being found at the surface of the blocks. As introduced in the magnetophoresis assembly theory, the convection of the Co NRs towards the Ni blocks required magnetic field gradients larger than the critical ones : 700 $T.m^{-1}$ along the rod long axis, *i.e.* $\vec{x}$, and 200 $T.m^{-1}$ perpendicularly to it, *i.e.* $\vec{y}$ and $\vec{z}$. The color scale used allows to directly visualize the regions where these conditions were fulfilled, the sign of the magnetic field gradients indicates the direction of the Co NR motion. Attraction zones are clearly visible along $\vec{x}$, while repulsion zones are determined at the direct vicinity of the Ni block facets along $\vec{y}$ and $\vec{z}$. The lateral extension of the attraction zone along $\vec{x}$, which eventually leads to the accumulation of Co NRs in the gap, is determined in Fig. 3b. For the three Ni block length studied, an attraction up to a distance of ~120 µm was obtained. The appearance of collective effects through Co NRs aggregation which leads to a decrease of critical field gradients would increase the size of the attraction. In the gap this may give to the capture of all particles present between the Ni blocks.

The Ni block length does affect the spatial extension of the repulsive zones observed along $\vec{y}$ and $\vec{z}$. Indeed, lower values of $\frac{\partial \overrightarrow{B_y}}{\partial x}$ and $\frac{\partial \overrightarrow{B_z}}{\partial x}$ were obtained for increased length. For instance, the repulsion zone observed vanished at the center of the blocks for $l = 500$ µm (Fig. 3c). This may affect the geometrical repartition of Co NRs within the final assembly.

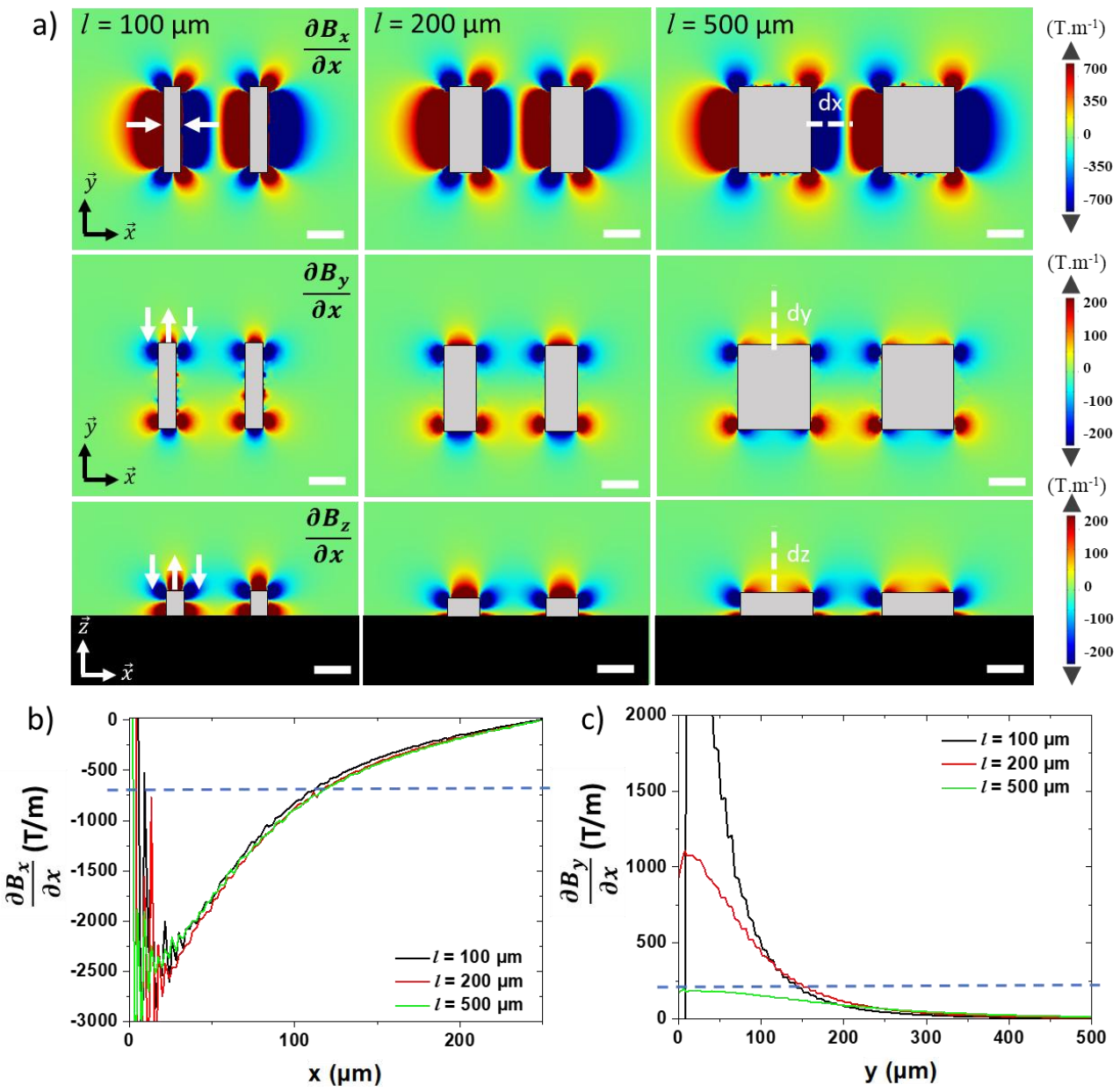

Figure 3: a) 2D mapping of the magnetic field gradients $\frac{\partial B_x}{\partial x}$ (first row), $\frac{\partial B_y}{\partial x}$ (second row) and $\frac{\partial B_z}{\partial x}$ (third row) induced by Ni blocks of 500 µm (w) × 150 µm (h) and a length l of 100 µm (left column), 200 µm (middle column) and 500 µm (right column) once magnetized under an external field $\mu_0 H_{ext}$ = 1 T. Scale bar = 200 µm. White arrows indicated for the 100 µm-length Ni block are guide to the eye for the attractive and repulsive zones felt by the Co NRs. White dashed lines depict the extension of the attraction (dx) and repulsion (dy, dz) zones. Magnetic field gradients b) $\frac{\partial B_x}{\partial x}$ and c) $\frac{\partial B_y}{\partial x}$ along the profile lines depicted on the 500 µm-length Ni block on a) (from the edge of the block). The spatial extension of the attractive and repulsive areas at the vicinity of Ni blocks were determined at the intersection of the simulated curve with the critical gradient value, represented by the dashed blue line.

Directed assembly of Co NRs with different Ni blocks.

A concentrated suspension of Co NRs dispersed in anisole ([Co] ~ 80 g/L) was drop casted on the patterned substrates. The external magnetic field $\mu_0 H_{ext}$ = 1T was then applied leading to the alignment and, within the attraction areas, to the motion of the Co NRs towards the Ni blocks. The excess of Co NRs, which never interact with the large magnetic field areas, and thus lead to nonspecific deposition, was washed away with chloroform. The deposition was repeated 6 times to fill the entire space between the Ni blocks. After the complete evaporation of the solvent, fairly conformal depositions were obtained for the three Ni block lengths (l = 100, 200, 500 and 1000 μm) as revealed by SEM images (Fig. 4a-c,e). XRD pattern revealed a fairly good alignment (Figure S2) as previously extensively reported.[30] For the first time, the Co assemblies were further investigated using X-Ray tomography, to probe the presence of internal porosity (Fig. 4d, Video S1). All the materials were seen as fully compact, thus not exhibiting any mesoscopic pores with sizes larger than 10 μm (resolution of the apparatus).

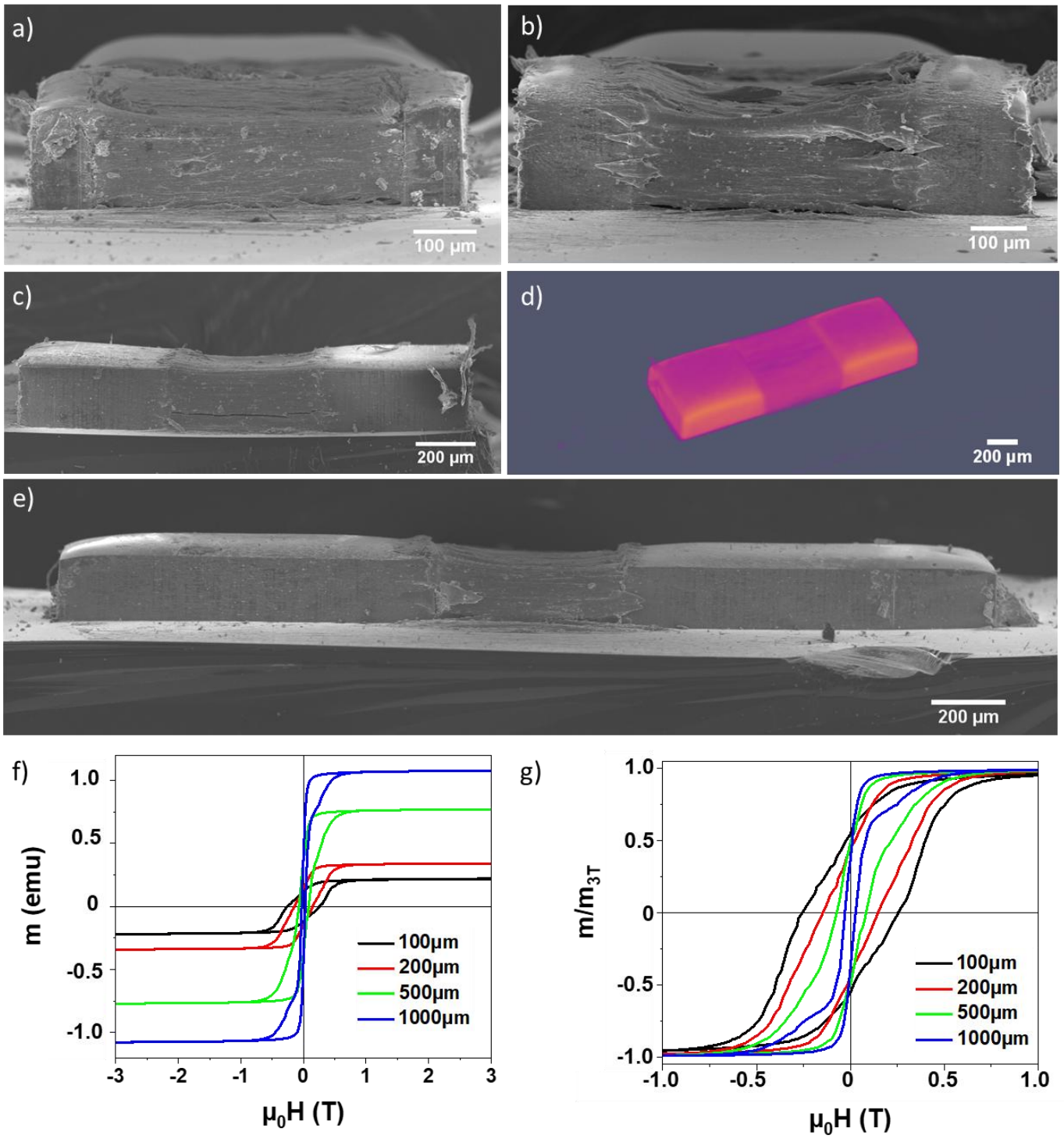

Figure 4. SEM images of the Ni-Co-Ni hybrid structures obtained with Ni block length *l* of a) 100, b) 200, c) 500 and e) 1000 µm. d) X-Ray tomography of the Ni-Co-Ni with and *l* = 500 µm. f-g) In-plane magnetization curves of the different structures measured at 300K along the x direction.

Magnetic properties of the hybrid Ni-Co-Ni structures.

The 300K magnetic properties of the hybrid Ni-Co-Ni structures were investigated using a VSM. As one could expect, the total moment increases with the Ni block length, due to the larger magnetic volume (Fig. 4f). However, the longer the Ni blocks, the more magnetic decoupling was observed. For l = 500 and 1000 µm a two-step hysteresis curve was evidenced (Fig. 4g). This reveals the magnetization reversal of the Ni blocks at low field, due to their soft nature; while the Co-based magnet only switches at larger fields. The quantification of the magnetic coupling strength between the Ni and the Co would deserve a detailed study combining recoil curves, MFM studies and micromagnetic simulations but this goes beyond the scope of the present study.

The coercive fields, summarized in Table 1, and the hysteresis shape being key parameters for the $(BH)_{max}$, the integration of such hybrid structures as integrated permanent magnet could therefore be questioned.

Using a Hall micro-probe, the magnetic induction generated by the hybrid Ni-Co-Ni structures along $\vec{x}$, as a function of the distance to the outer Ni block extremity D was measured (inset Fig. 5a). The results obtained for two extreme Ni block lengths of l = 100 µm and l = 1000 µm were compared (Fig. 5a). The magnetic stray fields were significantly reduced for large Ni volumes but could still be detected. For instance, at a distance of D = 200 µm, magnetic inductions of 19 mT and 10 mT were measured for l =100 and 1000 µm, respectively.

The experimental decay of the magnetic induction as a function of D was adjusted using finite element simulations. The hybrid Ni-Co-Ni structures were implemented considering the respective volume deduced from X-Ray tomography, while the magnetic volume fraction fv within the Co assembly was let as a free parameter. For both cases, the best adjustments were

obtained for a fv = 25%. Therefore, the modification of the Ni block length did not impact the Co NR assembly, the magnetic field gradients induced by the longest Ni blocks were sufficient to yield a fairly dense material. The magnetic volume fraction of 25%, that can be seen as surprisingly low, results from the composite nature of the starting Co NRs used. Indeed, the NRs being prepared by a wet chemistry approach under ambient conditions, they are composed of a metallic Co core, surrounded by a native Co oxide shell of ~1.2 nm, and an organic shell which was essential to promote the anisotropic growth.[28]

The magnetization curves measured at 300K were normalized respectively to the total magnetic volume of the hybrid structure, i.e. the Ni blocks and the Co assembly considering fv = 25% (Figure 5b). Interestingly, even though the magnetic inductions generated by the two magnets were fairly different, a similar remanent magnetization $\mu_0 M_r$ = 0.28T was found. For l = 1000 µm, this value resulted from the large total magnetization while for l = 100 µm, it arisen from the larger remanence ratio m_r/m_{3T} (Figure 4g and Table 1). Considering the magnetic volume fraction, $B(H)$ loop could be calculated and the $(BH)_{max}$ product estimated. As expected, the presence of the Ni blocks drastically reduces the permanent magnet performances leading to $(BH)_{max}$ values of 10 kJ.m^{-3} and 2 kJ.m^{-3} for l = 100 and 1000 µm respectively. The comparison between both hybrid structure clearly highlight the key importance of the $(BH)_{max}$ and not only of the remanent magnetization on the magnetic stray field delivered by the magnet. We previously reported $(BH)_{max}$ values of ~30kJ.m^{-3} for pure Co NR magnet, obtained after having manually removed the Ni blocks.[30]

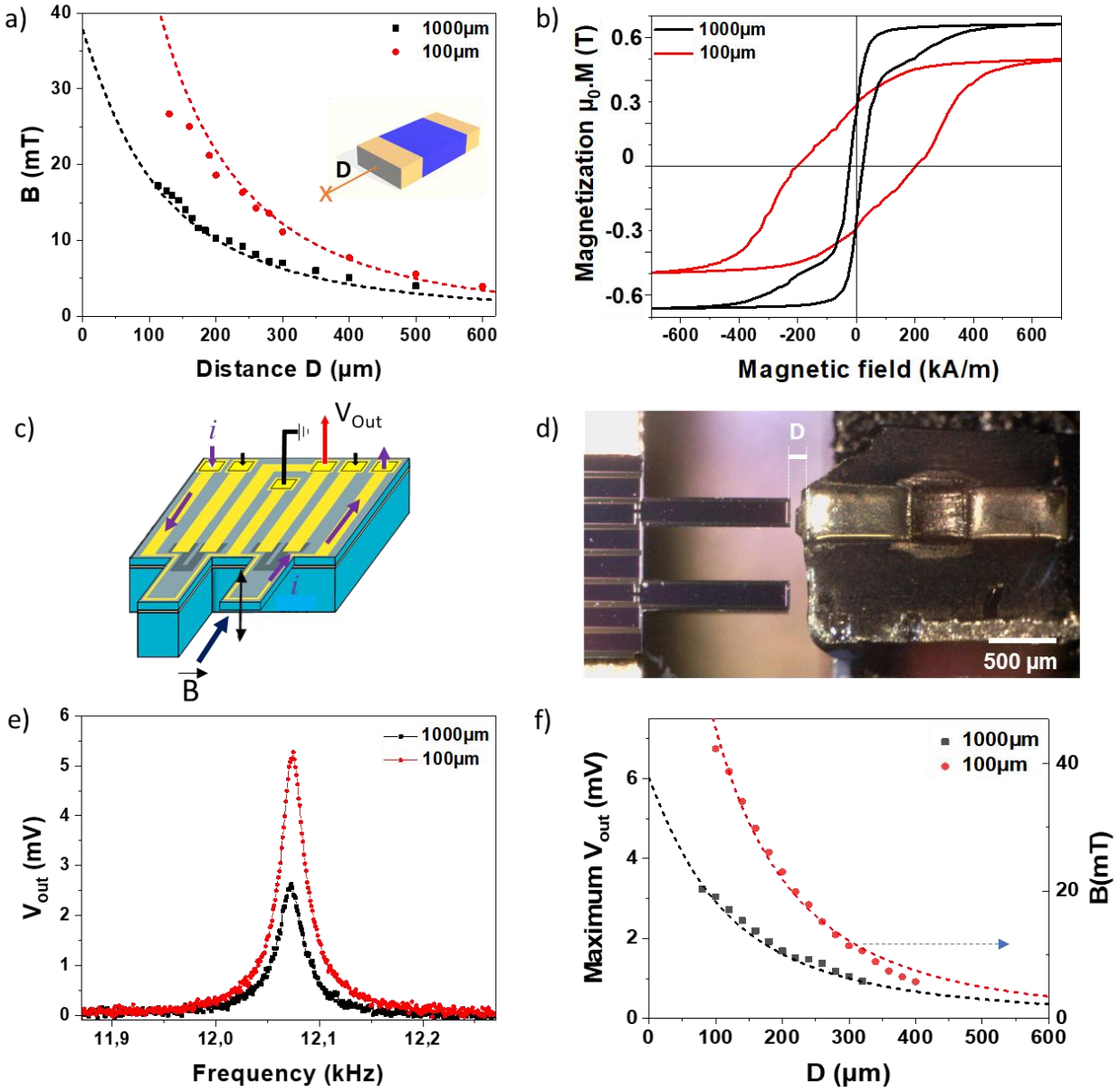

Figure 5. a) Evolution of the in-plane magnetic stray field as a function of the distance D to the hybrid Ni-Co-Ni structures as depicted in inset. (black : Ni length l = 1000 µm; red : l = 100 µm). Scatters : experimental values measured by a Hall microprobe, Dashed lines : Simulated induction considering a magnetic volume fraction f_v = 25%. b) Magnetic measurements recorded at 300K after magnetic volume normalization, considering f_v = 25%. c) Schematic view of a MEMS sensor consisted of a Si microcantilever electromagnetically actuated thanks to a AC current i and a magnetic field $\vec{B}$. d) Optical image of the hybrid Ni-Co-Ni structure (Ni length l = 1000 µm) placed in front of the microcantilever. e) Output signal of the actuated MEMS Si cantilever as a function of the AC current frequency, measured by means of the integrated piezoresistors for a distance D = 130 µm between the cantilever and the hybrid structure. As inset : optical image of hybrid Ni-Co-Ni structure (l =1000 µm) reported in front of the MEMS free standing cantilever. f) Scatters : evolution of the output signal that corresponds to the amplitude of vibration of the cantilever (maximum at the resonant frequency), as a function of the distance D. Dashed lines : simulated induction considering f_v = 25%.

Electromagnetic actuation of a MEMS sensor

A microelectromechanical system (MEMS) sensor consisting of a Si microcantilever (Fig. 5c) was used to study the potential application of the hybrid Ni-Co-Ni structures as integrated permanent magnets. The electromagnetic actuation of the cantilever vibration relies on the Laplace force induced at its extremity :

$$\overrightarrow{dF} = i\overrightarrow{dl} \times \vec{B} \text{ (Eq. 5)}$$

The amplitude of vibration was detected using integrated piezoresistors. The hybrid Ni-Co-Ni structures with Ni blocks of l = 100 µm and l = 1000 µm were placed in front of the cantilever at a distance D (Fig. 5d). The first resonance was clearly evidenced for both hybrid magnets at D = 130 µm (Fig. 5e). As expected, the amplitude of the resonance peak decreased with D, following the same decay as the magnetic induction induced by the hybrid structures (Fig. 5f). This similarity unambiguously proves that the electromagnetic actuation of the MEMS sensor was indeed induced by the hybrid structures.

Thus, the presence of the soft Ni blocks reduces the overall performances of the Co based magnet, in particular the $(BH)_{max}$ values, but are not prohibiting the potential use as integrated permanent magnet. To maintain proper performances, one should favor the smallest Ni blocks within the hybrid Ni-Co-Ni structures. However, a tradeoff between final properties and magnetic field gradients should be found. Indeed, decreasing further the Ni block length down to 50µm, while keeping a 500 µm gap, did not allow to assemble a dense Co-NR based material, due to the limited magnetic field gradient induced by such thin blocks.

Conclusion

Rare-earth free permanent magnets based on Co NRs were prepared using a magnetophoresis-driven capillary assembly process. To be effective and allow the integration

of magnets with controlled size, shape and at the proper position on nomadic devices, magnetically soft blocks are mandatory to induce local magnetic field gradients. The selective removal of these blocks being a complex task, their effect on the magnetic properties of the final hybrid Ni-Co-Ni magnets were determined. As expected, the presence of these soft regions drastically reduced the coercive field and the remanent magnetization of the PM, favouring the magnetization reversal within the structure. However, these hybrid Ni-Co-Ni were proven as being performant enough to actuate a gravimetric MEMS sensor, even at fairly large distances, thanks to the long-range magnetic induction they induce. For instance, the hybrid Ni-Co-Ni magnets with Ni block length l = 100 µm generated a magnetic induction of 19 mT at a distance of 200 µm. Thus, keeping the soft magnet volume as low as possible, the direct integration of Co NRs based magnets assembled by magnetophoresis is a promising alternative approach to the reported rare-earth based PM classically used. The proof of concept of the direct integration of the Co NR magnets in the process flow of a microsystem within a clean room facility is currently under investigation.

Experimental Section

Synthesis of Co NRs. Cobalt nanorods were produced by the polyol process following a procedure previously described.[28] Briefly, cobalt laurate ([Co] = 8×10^{-2} mol.L^{-1}) was dispersed in a basic solution of 1,2-butanediol ([NaOH] = 7.5×10^{-2} mol.L^{-1}) under air. Ruthenium chloride was added to promote the nucleation step ([Ru]/[Co] = 2.5%). The suspension, placed in a quadricol, was heated under mechanical stirring at a rate of 8°C /min up to 175°C using a classic heating mantle. The reaction was allowed to react 20 min before cooling down to room temperature. As previously reported, the shape of the NRs varied with the mechanical stirring speed, larger tips being obtained at higher speed.[34] The obtained Co NRs exhibit a 1.2 nm thick Co oxide shell which serve as a passivating layer.

Co NR characterization. The particles were characterized by transmission electron microscopy (TEM), using a 100 kV Jeol JEM 1011. The particles were recovered by

centrifugation, washed four times with chloroform. A drop of the colloidal solution of Co nanorods in chloroform was deposited on a carbon coated copper grid. Image analysis on ~200 rods using the ImageJ software was performed to determine the Co NR mean diameter and length. X-ray diffraction (XRD) patterns were recorded on a PANalytical Empyrean diffractometer using the Co K_α radiation.

Preparation of concentrated Co NR suspension. Co NRs were retrieved from the reaction medium using conventional purification process under air. Typically, 10 mL of chloroform was added to 5 mL of the mother liquor solution. After 5 min of sonication, the particles were magnetically attracted. The supernatant was discarded and the precipated particles redispersed in 10 mL of chrloroform. The purification was repeated four times. The NRs were finally redispersed into 300 µL of anisole leading to a Co suspension with an estimated concentration of approximatively 80 g/L.

Electroplating of Ni blocks. Ni blocks of length varying from 100 µm to 1000 µm were prepared by conventional microfabrication procedure, as previously reported.[30] Briefly, a conductive seed layer (100 nm Ti / 200 nm Cu) was evaporated onto a 4-inches Si wafer and covered by a 200 µm thick dry film elaborated via lamination at 100°C of two 100 µm negative films of WBR 2100 (Dupont). This thick film, which serves as mold for the electrodeposition was patterned by photolithography (power: 1.5 J/cm²; λ = 365 nm; development: 20 min in Na_2CO_3 developer, room temperature). 150 µm-thick Ni was then electroplated at a speed corresponding to 0.7 µm/min using a Yamamoto cell plating with NB Semi Plate Ni 100 bath (NB Technology). The resist was finally removed using NF52 photoresist stripper (TechniStrip) at 70 °C during 25 min and the Cu/Ti seed layer was etched using sulfuric acid and hydrogen peroxide (1% of each), and a 5 % hydrofluoric acid solution.

Magnetophoresis experiment. The Si sample patterned with Ni blocks was introduced in a Teflon mold and placed in an electromagnet generating a uniform magnetic field ($\mu_0 H_{app}$). The deposition of the Co NRs was performed following a three-step process previously reported.[30] Briefly, *i*) 10 µL of the concentrated suspension was deposited at $\mu_0 H_{app} = 0$; *ii*) alignment of Co NRs and attraction by the Ni blocks at $\mu_0 H_{app} = 1$T; *iii*) washing of the Co NRs excess with 500 µL of chloroform, keeping $\mu_0 H_{app} = 1$T. The impregnation was classically repeated three times, before allowing the solvent evaporating at room temperature

and atmospheric pressure. To fully fill up the gap between the Ni blocks, the deposition process (3 impregnations and 1 evaporation) was repeated twice.

Structural and magnetic characterizations of the hybrid Ni-Co-Ni PM. Scanning electron microscopy (SEM) was performed using a JEOL JSM 7800F. For X-Ray tomography measurement, the acquisition of the tilt series was performed on a Nikon XT V 130kV, working at 55kV/30µA. 1800 projections were recorded over the full 360° range with a 0.2° step and a 32frame/projection resolution using the InspectX software. CTPro3D and Tomviz softwares were used for the reconstruction and the vizualisation, respectively.

The magnetic properties were characterized using a Physical Property Measurement System (PPMS, Quantum Design) in the Vibrating Sample Magnetometer configuration (VSM). 3T Hysteresis measurements in parallel configuration were recorded at room temperature on hybrid Ni-Co-Ni PM and pure Co-NR assembly after removal of the Ni blocks.

The magnetic volume fraction f_v within the Co NR assembly was calculated from the saturation moment m_S recorded at 3T (expressed in emu), the assembly volume estimated by SEM (expressed in cm^3) and the expected bulk magnetization (for Co : $M_{S,Co\ bulk}$ = 1440 $kA.m^{-1}$)[6] as follow :

$$f_v = \frac{M_{S,exp}(kA.m^{-1})}{M_{S,Co\ bulk}(kA.m^{-1})} \quad \text{(Eq.1)}$$

$$\text{where } M_{S,exp}(kA.m^{-1}) = M_{S,exp}(emu.cm^{-3}) = \frac{m_S(emu)}{V(cm^3)} \text{ (Eq. 2)}$$

For the hybrid Ni-Co-Ni PM, the recorded moment m (emu) was converted in SI unit ($kA.m^{-1}$) considering the constituting Ni and Co volume (V_{Ni}, V_{Co}) determined by SEM (expressed in cm^3), the magnetic volume fraction f_v and the magnetization ($M_{S,Ni}$ = 500 $kA.m^{-1}$) as follow :

$$M(kA.m^{-1}) = \frac{m(emu)}{m_s}\left[\left(\frac{V_{Ni}}{V_{Ni}+V_{Co}}.M_{s,Ni}\right) + \left(\frac{V_{Co}}{V_{Ni}+V_{Co}}.M_{s,Co\ bulk}.f_v\right)\right] \quad \text{(Eq.3)}$$

B(H) loop was extrapolated considering: $B = \mu_0(H + M)$ (Eq. 4), allowing to determine the energy product $(BH)_{max}$.

The magnetic induction profile as a function of the PM distance was experimentally mapped using a Hall-effect micro-probe mounted on a moving stage.[35] The Hall constant of the micro-probe (k = 200 $\Omega.T^{-1}$) was preliminary calibrated using the gaussmeter BGM 101 (Brockhaus Measurements).

MEMS actuation. As previously reported, rheological MEMS sensors consisting of two cantilevers (a reference and a freestanding) were used.[30] The freestanding cantilever was actuated by the electromagnetic Lorentz force, thanks to a sinusoidal AC current driven in the conducting path patterned onto the cantilevers and the static magnetic field generated by the hybrid Ni-Co-Ni PM or the Co-NR based PM. The vibration amplitude was detected through piezoresistors integrated at the clamped-end of the cantilevers and converted into an output voltage thanks to a transimpedance amplifier.

Finite Element simulations. The magnetic field gradients induced by the different Ni blocks were simulated using Comsol Multiphysics 4.3. The magnetic induction in a 4 mm^3 air box (50 µm mesh size) was determined from the Maxwell equation in stationary regime using the *Magnetic Field No Current* (MFNC) module. The uniform magnetic field generated by the electromagnet was implemented *via* the introduction of magnetic potentials (1600 A/m) at the box surfaces. The magnetization of the Ni blocks with the appropriate sizes was specified from experimental measurements. The 3D magnetic induction gradients were calculated using the *Coefficient Form PDE* module.

Acknowledgments:

This study has been partially supported through the French national project POMADE (ANR 19-CE09-0021-01), the EUR grant NanoX n° ANR-17-EURE-0009 in the framework of the « Programme des Investissements d'Avenir" and the prematuration program of the Région Occitanie (AimCap). This work has been partly supported by the technology platform of LAAS-CNRS and the French RENATECH network. PM and AG thanks the Région Occitanie and the Université Fédérale de Toulouse for phD funding. Angélique Gillet and Adeline Pham are warmly thanked for their help for chemical synthesis.

Conflict of Interest:

The authors have no conflict of interest

TOC image :

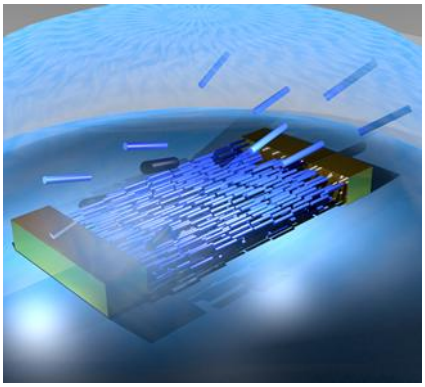

Integrated permanent magnets were prepared by directed assembly of Co nanorods driven by magnetophoresis. The resulting hybrid Ni-Co-Ni magnets allows to actuate a MEMS gravimetric sensor.

References:

(1) Silveyra, J. M.; Ferrara, E.; Huber, D. L.; Monson, T. C. Soft Magnetic Materials for a Sustainable and Electrified World. *Science* **2018**, *362* (6413), eaao0195. https://doi.org/10.1126/science.aao0195.

(2) Gutfleisch, O.; Willard, M. A.; Brück, E.; Chen, C. H.; Sankar, S. G.; Liu, J. P. Magnetic Materials and Devices for the 21st Century: Stronger, Lighter, and More Energy Efficient. *Adv. Mater.* **2011**, *23* (7), 821–842. https://doi.org/10.1002/adma.201002180.

(3) Mohd Ghazali, F. A.; Hasan, M. N.; Rehman, T.; Nafea, M.; Mohamed Ali, M. S.; Takahata, K. MEMS Actuators for Biomedical Applications: A Review. *J. Micromechanics Microengineering* **2020**, *30* (7), 073001. https://doi.org/10.1088/1361-6439/ab8832.

(4) Roy, S.; Mallick, D.; Paul, K. MEMS-Based Vibrational Energy Harvesting and Conversion Employing Micro-/Nano-Magnetics. *IEEE Trans. Magn.* **2019**, 1–15. https://doi.org/10.1109/TMAG.2019.2896105.

(5) Jones, N. The Pull of Stronger Magnets. *Nature* **2011**, *472*, 22–23.

(6) Coey, J. M. D. *Magnetism and Magnetic Materials*; Cambridge University Press: Cambridge, 2010.

(7) Arnold, D. P.; Naigang Wang. Permanent Magnets for MEMS. *J. Microelectromechanical Syst.* **2009**, *18* (6), 1255–1266. https://doi.org/10.1109/JMEMS.2009.2034389.
(8) Walther, A.; Marcoux, C.; Desloges, B.; Grechishkin, R.; Givord, D.; Dempsey, N. M. Micro-Patterning of NdFeB and SmCo Magnet Films for Integration into Micro-Electro-Mechanical-Systems. *J. Magn. Magn. Mater.* **2009**, *321* (6), 590–594.
(9) Kustov, M.; Laczkowski, P.; Hykel, D.; Hasselbach, K.; Dumas-Bouchiat, F.; O'Brien, D.; Kauffmann, P.; Grechishkin, R.; Givord, D.; Reyne, G.; Cugat, O.; Dempsey, N. M. Magnetic Characterization of Micropatterned Nd–Fe–B Hard Magnetic Films Using Scanning Hall Probe Microscopy. *J. Appl. Phys.* **2010**, *108* (6), 063914. https://doi.org/10.1063/1.3486513.
(10) Keller, F. O.; Haettel, R.; Devillers, T.; Dempsey, N. M. Batch Fabrication of 50 Lm Thick Anisotropic Nd-Fe-B Micromagnets. *IEEE Trans. Magn.* **2021**, 1–1. https://doi.org/10.1109/TMAG.2021.3101911.
(11) Dumas-Bouchiat, F.; Zanini, L. F.; Kustov, M.; Dempsey, N. M.; Grechishkin, R.; Hasselbach, K.; Orlianges, J. C.; Champeaux, C.; Catherinot, A.; Givord, D. Thermomagnetically Patterned Micromagnets. *Appl. Phys. Lett.* **2010**, *96* (10), 102511. https://doi.org/10.1063/1.3341190.
(12) Cao, Y.; Sheng, Y.; Edmonds, K. W.; Ji, Y.; Zheng, H.; Wang, K. Deterministic Magnetization Switching Using Lateral Spin–Orbit Torque. *Adv. Mater.* **2020**, *32* (16), 1907929. https://doi.org/10.1002/adma.201907929.
(13) Han, M.; Li, Z.; Sun, X.; Zhang, H. Analysis of an In-Plane Electromagnetic Energy Harvester with Integrated Magnet Array. *Sens. Actuators Phys.* **2014**, *219*, 38–46. https://doi.org/10.1016/j.sna.2014.08.008.
(14) Rhen, F. M. F.; Coey, J. M. D. Electrodeposition of Coercive L10 FePt Magnets. *J. Magn. Magn. Mater.* **2010**, *322* (9–12), 1572–1575. https://doi.org/10.1016/j.jmmm.2009.09.027.
(15) Wang, Y.; Ewing, J.; Arnold, D. P. Ultra-Thick Electroplated CoPt Magnets for MEMS. *J. Microelectromechanical Syst.* **2019**, *28* (2), 311–320. https://doi.org/10.1109/JMEMS.2018.2888846.
(16) Kandpal, M.; Sharan, C.; Palaparthy, V.; Tiwary, N.; Poddar, P.; Rao, V. R. Spin-Coatable, Photopatternable Magnetic Nanocomposite Thin Films for MEMS Device Applications. *RSC Adv* **2015**, *5* (104), 85741–85747. https://doi.org/10.1039/C5RA15706D.
(17) Huber, C.; Abert, C.; Bruckner, F.; Groenefeld, M.; Schuschnigg, S.; Teliban, I.; Vogler, C.; Wautischer, G.; Windl, R.; Suess, D. 3D Printing of Polymer-Bonded Rare-Earth Magnets With a Variable Magnetic Compound Fraction for a Predefined Stray Field. *Sci. Rep.* **2017**, *7* (1), 9419. https://doi.org/10.1038/s41598-017-09864-0.
(18) Descamps, L.; Mekkaoui, S.; Audry, M.-C.; Deman, A.-L.; Le Roy, D. Optimized Process for the Fabrication of PDMS Membranes Integrating Permanent Micro-Magnet Arrays. *AIP Adv.* **2020**, *10* (1), 015215. https://doi.org/10.1063/1.5129919.
(19) Li, H.; Flynn, T. J.; Nation, J. C.; Kershaw, J.; Scott Stephens, L.; Trinkle, C. A. Photopatternable NdFeB Polymer Micromagnets for Microfluidics and Microrobotics Applications. *J. Micromechanics Microengineering* **2013**, *23* (6), 065002. https://doi.org/10.1088/0960-1317/23/6/065002.
(20) Panagiotopoulos, I.; Fang, W.; Ott, F.; Boué, F.; Aït-Atmane, K.; Piquemal, J.-Y.; Viau, G. Packing Fraction Dependence of the Coercivity and the Energy Product in Nanowire Based Permanent Magnets. *J. Appl. Phys.* **2013**, *114* (14), 143902. https://doi.org/10.1063/1.4824381.

(21) Oniku, O. D.; Bowers, B. J.; Shetye, S. B.; Wang, N.; Arnold, D. P. Permanent Magnet Microstructures Using Dry-Pressed Magnetic Powders. *J. Micromechanics Microengineering* **2013**, *23* (7), 075027. https://doi.org/10.1088/0960-1317/23/7/075027.
(22) Jackson, N.; Pedrosa, F. J.; Bollero, A.; Mathewson, A.; Olszewski, O. Z. Integration of Thick-Film Permanent Magnets for MEMS Applications. *J. Microelectromechanical Syst.* **2016**, *25* (4), 716–724. https://doi.org/10.1109/JMEMS.2016.2574958.
(23) Mohapatra, J.; Xing, M.; Elkins, J.; Beatty, J.; Liu, J. P. Extraordinary Magnetic Hardening in Nanowire Assemblies: The Geometry and Proximity Effects. *Adv. Funct. Mater.* **2021**, 2010157. https://doi.org/10.1002/adfm.202010157.
(24) Soulantica, K.; Wetz, F.; Maynadié, J.; Falqui, A.; Tan, R. P.; Blon, T.; Chaudret, B.; Respaud, M. Magnetism of Single-Crystalline Co Nanorods. *Appl. Phys. Lett.* **2009**, *95* (15), 152504. https://doi.org/10.1063/1.3237157.
(25) Soumare, Y.; Garcia, C.; Maurer, T.; Chaboussant, G.; Ott, F.; Fiévet, F.; Piquemal, J.-Y.; Viau, G. Kinetically Controlled Synthesis of Hexagonally Close-Packed Cobalt Nanorods with High Magnetic Coercivity. *Adv. Funct. Mater.* **2009**, *19* (12), 1971–1977. https://doi.org/10.1002/adfm.200800822.
(26) Gandha, K.; Elkins, K.; Poudyal, N.; Liu, X.; Liu, J. P. High Energy Product Developed from Cobalt Nanowires. *Sci. Rep.* **2014**, *4*. https://doi.org/10.1038/srep05345.
(27) Pousthomis, M.; Anagnostopoulou, E.; Panagiotopoulos, I.; Boubekri, R.; Fang, W.; Ott, F.; Atmane, K. A.; Piquemal, J.-Y.; Lacroix, L.-M.; Viau, G. Localized Magnetization Reversal Processes in Cobalt Nanorods with Different Aspect Ratios. *Nano Res.* **2015**, *8* (7), 2231–2241. https://doi.org/10.1007/s12274-015-0734-x.
(28) Anagnostopoulou, E.; Grindi, B.; Lacroix, L.-M.; Ott, F.; Panagiotopoulos, I.; Viau, G. Dense Arrays of Cobalt Nanorods as Rare-Earth Free Permanent Magnets. *Nanoscale* **2016**, *8* (7), 4020–4029. https://doi.org/10.1039/C5NR07143G.
(29) Ener, S.; Anagnostopoulou, E.; Dirba, I.; Lacroix, L.-M.; Ott, F.; Blon, T.; Piquemal, J.-Y.; Skokov, K. P.; Gutfleisch, O.; Viau, G. Consolidation of Cobalt Nanorods: A New Route for Rare-Earth Free Nanostructured Permanent Magnets. *Acta Mater.* **2018**, *145*, 290–297. https://doi.org/10.1016/j.actamat.2017.12.009.
(30) Moritz, P.; Gonon, A.; Blon, T.; Ratel-Ramond, N.; Mathieu, F.; Farger, P.; Asensio-Revert, J.-M.; Cayez, S.; Bourrier, D.; Saya, D.; Nicu, L.; Viau, G.; Leïchlé, T.; Lacroix, L.-M. Magnetophoresis-Assisted Capillary Assembly: A Versatile Approach for Fabricating Tailored 3D Magnetic Supercrystals. *ACS Nano* **2021**, *15* (3), 5096–5108. https://doi.org/10.1021/acsnano.0c10215.
(31) Cai, K.; Yang, M.; Ju, H.; Wang, S.; Ji, Y.; Li, B.; Edmonds, K. W.; Sheng, Y.; Zhang, B.; Zhang, N.; Liu, S.; Zheng, H.; Wang, K. Electric Field Control of Deterministic Current-Induced Magnetization Switching in a Hybrid Ferromagnetic/Ferroelectric Structure. *Nat. Mater.* **2017**, *16* (7), 712–716. https://doi.org/10.1038/nmat4886.
(32) Cao, Y.; Rushforth, AndrewW.; Sheng, Y.; Zheng, H.; Wang, K. Tuning a Binary Ferromagnet into a Multistate Synapse with Spin–Orbit- Torque- Induced Plasticity. *Adv. Funct. Mater.* **2019**, *29* (25), 1808104. https://doi.org/10.1002/adfm.201808104.
(33) De Las Cuevas, G.; Faraudo, J.; Camacho, J. Low-Gradient Magnetophoresis through Field-Induced Reversible Aggregation. *J. Phys. Chem. C* **2008**, *112* (4), 945–950. https://doi.org/10.1021/jp0755286.
(34) Mrad, K.; Schoenstein, F.; Nong, H. T. T.; Anagnostopoulou, E.; Viola, A.; Mouton, L.; Mercone, S.; Ricolleau, C.; Jouini, N.; Abderraba, M.; Lacroix, L.-M.; Viau, G.; Piquemal, J.-Y. Control of the Crystal Habit and Magnetic Properties of Co

Nanoparticles through the Stirring Rate. *CrystEngComm* **2017**, *19* (25), 3476–3484. https://doi.org/10.1039/C7CE00714K.

(35) Shaw, G.; Kramer, R. B. G.; Dempsey, N. M.; Hasselbach, K. A Scanning Hall Probe Microscope for High Resolution, Large Area, Variable Height Magnetic Field Imaging. *Rev. Sci. Instrum.* **2016**, *87* (11), 113702. https://doi.org/10.1063/1.4967235.